Research Square

Preprints are preliminary reports that have not undergone peer review.
They should not be considered conclusive, used to inform clinical practice,
or referenced by the media as validated information.

Polyvinylpyrrolidone-Derived Nitrogen-Doped Carbon as an Iodine Cathode Host for Aqueous Zinc-Iodine Batteries

Jiale Xu
Kunming University of Science and Technology
Li Wang
Hebei Minzu Normal University
Liu Chen
Kunming University of Science and Technology
Bo Jin
Southwest United Graduate School
Yin li
510527335@qq.com
Kunming University of Science and Technology
Yunke Wang
Yunnan Open University
Yaochun Yao
Kunming University of Science and Technology

Research Article

Keywords: Aqueous zinc-iodine battery, Nitrogen-doped carbon, Microporous carbon host, Shuttle effect

Posted Date: November 23rd, 2026

DOI: https://doi.org/10.21203/rs.3.rs-11256417/v1

License: This work is licensed under a Creative Commons Attribution 4.0 International License.
Read Full License

Additional Declarations: No competing interests reported.

Polyvinylpyrrolidone-Derived Nitrogen-Doped Carbon as an Iodine Cathode Host for Aqueous Zinc-Iodine Batteries

Jiale Xu[a], Li Wang[b], Chen Liu[a], Bo Jin[a], Yin Li[a*], Yunke Wang[c], Yaochun Yao[a*]

(a The National Engineering Laboratory for Vacuum Metallurgy, School of Metallurgical and Energy Engineering, Kunming University of Science and Technology, Kunming 650093, China;

b Hebei Key Laboratory of Smart Campus Management for Carbon Peaking and Carbon Neutrality, Hebei Minzu Normal University, Chengde 067002, China;

c Yunnan Open University, Kunming 650093, PR China)

Abstract: Aqueous zinc-iodine batteries (AZIBs) have the advantages of high safety, low cost, and environmental friendliness, but face challenges in practical applications such as severe polyiodide shuttle effects, poor electrical properties of iodine, and slow redox kinetics. To overcome these obstacles, this study used polyvinylpyrrolidone (PVP) as a carbon/nitrogen source to successfully synthesize nitrogen-doped microporous carbon nanosheets (NC-T) through a freeze-drying and high-temperature pyrolysis strategy. Results show that NC-650 prepared at 650°C has an ultra-high specific surface area of 992.74 $m^2 g^{-1}$ and a rich micropore distribution (1-2 nm), providing ample physical confinement space for iodine molecules and effectively buffering their volume expansion. In addition, in-situ doped active nitrogen sites enhance the adsorption of polyiodides through strong chemical anchoring effects and significantly improve interfacial charge transfer rates. Electrochemical performance evaluation shows that NC-650/I_2 exhibits a high specific capacity of 161.49 mAh g^{-1} at a current density of 0.1 A g^{-1} and excellent rate performance. Remarkably, after 3000 cycles at a high current of 1.0 A g^{-1}, the battery can still retain 83.6% of its initial capacity, with the coulombic efficiency consistently close to 100%. This study provides a new design idea for developing long-life, highly stable, high-performance AZIBs through microstructural adjustment and chemical active site design.

Keywords: Aqueous zinc-iodine battery; Nitrogen-doped carbon; Microporous carbon host;

* Corresponding author: Yin Li, Yaochun Yao
National Engineering Laboratory of Vacuum Metallurgy, Kunming University of Science and Technology, Kunming 650093, Yunnan province, China
Tel/fa: +86-871-65161583
E-mail address: 510527335@qq.com (Dr. Y. Li), yaochun9796@163.com (Pro. Y. Yao)

Shuttle effect

1. Introduction

Under the grand paradigm of the global energy structure transition and the "Dual Carbon" goals (carbon peak and carbon neutrality), the development of large scale energy storage technologies characterized by high safety, low cost, and extended cycle life has emerged as a primary research focus within the field of energy materials [1-3]. Among various candidates, aqueous rechargeable zinc-ion batteries (ZIBs) have garnered significant attention due to their intrinsic safety, high crustal abundance, and environmental friendliness [4-6]. Within the landscape of aqueous energy storage systems, the zinc-iodine ($Zn-I_2$) battery has emerged as a preeminent device candidate for low-cost energy storage [7]. This prominence is attributed to the cost-effectiveness and abundance of iodine, coupled with its high theoretical specific capacity (211 mAh g^{-1}) and a suitable operating voltage (1.3 V) [8, 9]. However, inherent deficiencies such as the poor electronic conductivity of insulating iodine, the sluggish kinetics of the solid-liquid-solid phase transition reaction (iodine reduction reaction, IRR), and, most critically, the detrimental "shuttle effect" of polyiodide species hinder their practical commercialization [10-13]. During charge-discharge cycles, the cathode generates highly water-soluble polyiodide intermediates (e.g., I_3^-, I_5^-) [14-16]. Driven by concentration gradients, these polar species readily traverse the separator and migrate to the zinc anode, triggering irreversible chemical corrosion and self-discharge [17]. This not only causes a severe loss of active material, but also leads to a cliff-like drop in battery coulombic efficiency and a shortened cycle life [18-20]. In addition, the intrinsic poor conductivity of iodine and slow reaction kinetics result in low active material utilization and poor rate performance [21, 22]. To address these issues, the preparation of ideal host materials for iodine is crucial. Among many candidate materials, carbon-based frameworks are favored for their excellent conductivity and tunable structures [12, 13]. As an iodine carrier material, porous carbon plays a key inhibitory role in the dissolution and shuttling of iodine and polyiodides through its pore structure via physical confinement effects. Micropores mainly restrict the shuttling effect and stabilize iodine, mesopores promote ion transport and buffer volume changes, and macropores accelerate electrolyte infiltration and provide structural support [23-25]. However, the interaction between non-polar pure carbon materials and polar polyiodides is relatively weak, making it difficult to completely eliminate the shuttle effect [26, 27]. Li et al. proposed introducing highly electronegative nitrogen atoms into porous carbon materials to dope

the carbon lattice, which can not only break the electrical neutrality of carbon atoms, endow the framework with abundant polar chemical adsorption sites, but also optimize the local electron distribution and effectively reduce the reaction barrier for iodine species conversion [28-30]. Similarly, Liu et al. further analyzed the electrocatalytic activity of nitrogen configurations and clearly established the structure–activity relationship between nitrogen configurations and iodine catalytic activity [23, 31]. Therefore, preparing suitable nitrogen-rich precursors to construct porous heteroatom-doped carbon networks is an ideal approach to achieve physical confinement, chemical anchoring, and catalytic acceleration.

Hence, in this study, we selected polyvinylpyrrolidone (PVP)-a polymer rich in pyrrolidonic rings-as a dual-source precursor for both carbon and nitrogen. Utilizing a combination of freeze-drying and high-temperature activation/calcination processes, we successfully synthesized nitrogen-doped microporous carbon nanosheets (NC-T) featuring a highly developed pore architecture. Through the precise regulation of activation temperatures, an optimized configuration of nitrogen-doping content and specific surface area within the NC-T framework was achieved. Furthermore, the electrochemical behavior of the resulting materials as cathode hosts for Zn-I_2 batteries was systematically evaluated. Investigations reveal that the as-prepared NC-T sheet-like porous carbon provides vast physical confinement space for the uniform loading of elemental iodine and the accommodation of its volume expansion, owing to its ultra-high specific surface area and abundant microporous networks. More significantly, the highly active nitrogen-doping sites facilitate strong chemical bonding with polyiodides, thereby fundamentally suppressing the transmembrane shuttle effect of the active species. Benefiting from the synergistic effects of this structural and compositional design, the optimized NC-650/I_2 composite cathode demonstrates exceptional rate capability and ultra-long cycling stability within Zn-I_2 battery systems.

2. Experimental section

2.1 Preparation of Nitrogen-Doped Microporous Carbon Materials

Initially, 1.0 g of polyvinylpyrrolidone (PVP, Mw= 24,000) was dissolved in 15 mL of saturated NaCl solution under vigorous stirring. The resulting solution was frozen and subjected to lyophilization to yield a xerogel. Subsequently, the obtained xerogel was mixed and ground with $ZnCl_2$ at a weight ratio of 1:2. The mixture was then placed in a muffle furnace and pyrolyzed at 600, 650, and 700°C for 2 h under a N_2 atmosphere. After cooling to room temperature, the collected

products were immersed in a 1 M H_2SO_4 solution and stirred for 12 h to obtain the nitrogen-doped microporous carbon nanosheets, denoted as NC-600, NC-650, or NC-700, respectively.

2.2 Synthesis of NC/I_2 Composites

Nitrogen-doped microporous carbon/iodine (NC-T/I_2) composites are synthesized via a vapor-phase melt-diffusion method. Specifically, 0.15 g of NC-600, NC-650, or NC-700 and 0.2 g of elemental iodine are weighed and ground in a mortar for 20 min. The mixture is then transferred to a Teflon-lined stainless steel autoclave, sealed, and maintained at 130°C in an oven for 5 h. After cooling to room temperature, the composites are further treated at 80°C for 3 h in air to remove any excess iodine adhering to the external surface. The resulting final products were designated as NC-600/I_2, NC-650/I_2, and NC-700/I_2, respectively. The preparation process is shown in Fig. 1.

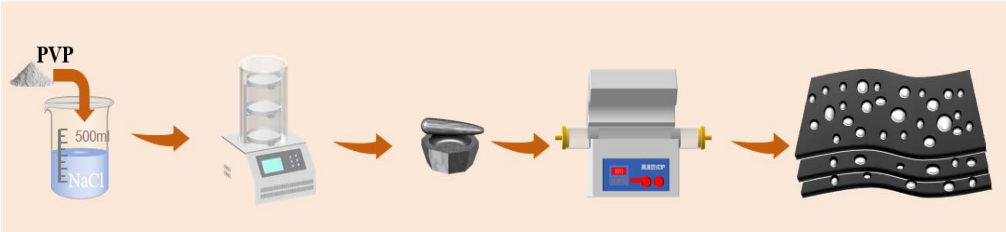

Fig. 1 Schematic illustration of the synthesis process of NC-T.

2.3. Characterization

X-ray diffraction (XRD) patterns were obtained by a Rigaku D/MAX-2550-PC X-ray diffractometer. The pore size distribution and specific surface area of the samples were calculated from nitrogen adsorption/desorption isotherms (Autosorb IQ Station) that were obtained using a Barrett-Joyner-Halenda (BJH) and Brunauer-Emmett-Teller (BET) method, respectively. The structure and morphology of the samples were characterized by using scanning electron microscopy (SEM, SU8010) with energy-dispersive X-ray spectroscopy (EDX). Raman spectra were collected on a Renishaw in Via using a laser with an excitation wavelength of 532 nm. X-ray photoelectron spectroscopy (XPS) analysis was performed on Thermo Scientific K-Alpha. Thermogravimetric analysis (TGA) was performed on a Pyris 1 TGA (PerkinElmer) System under N_2 flow (50-800°C, 10°C min^{-1}).

2.4 Electrochemical measurement

The cathode electrodes were prepared by mixing the as-synthesized composite, Ketjen black, and polyvinylidene fluoride (PVDF) at a weight ratio of 8:1:1 in N-methyl-2-pyrrolidone (NMP). After grinding for 30 min, the resulting homogeneous slurry was coated onto a 100 μm-thick

titanium (Ti) foil and dried in a vacuum oven at 60°C for 12 h. The coated current collector was subsequently punched into circular electrodes with a diameter of 14 mm. The coin cells were assembled using the prepared electrodes as the cathode, a zinc foil (12 mm in diameter) as the anode, and glass fiber as the separator, with 2.0 M $ZnSO_4$ solution serving as the electrolyte. The mass loading of the active material was approximately 0.8-1.2 mg cm^{-2}.

Galvanostatic charge-discharge (GCD) tests were conducted on a LANHE CT-2001A battery testing system within a voltage window of 0.6-1.6 V. Cyclic voltammetry (CV) and electrochemical impedance spectroscopy (EIS) measurements were performed using a CHI660E electrochemical workstation (Shanghai Chenhua Instrument Co., Ltd.).

3 Results and discussion.

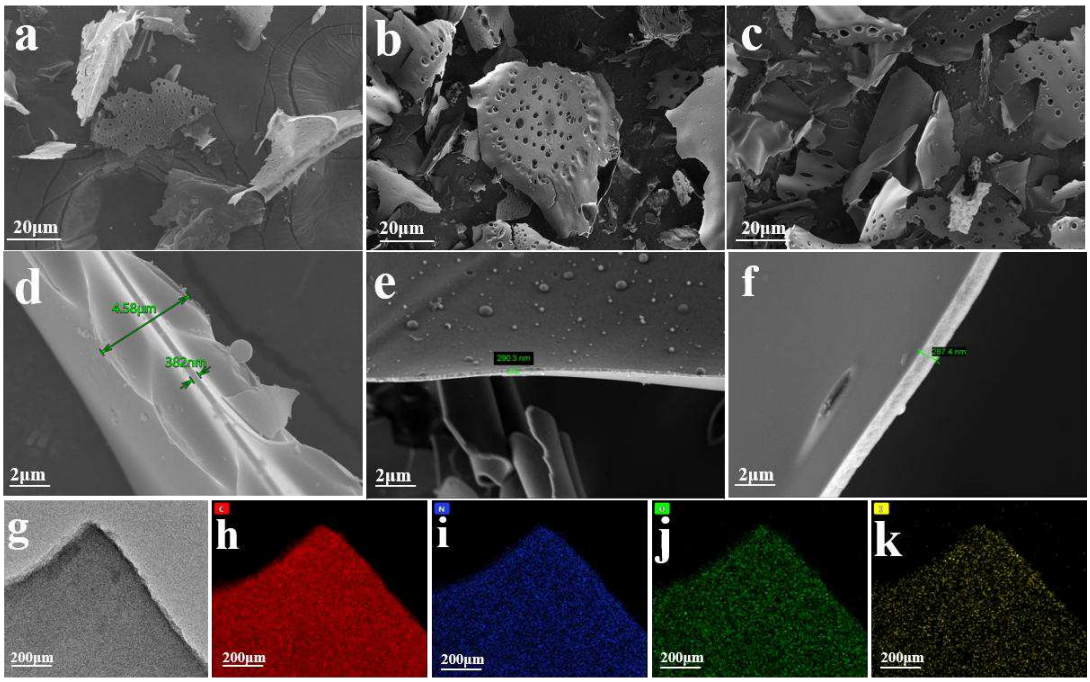

Fig. 2 (a-c) SEM of NC-600, NC-650 and NC-700; (c-f) Thickness of NC-600, NC-650 and NC-700; (g) TEM of NC-650/I_2; (h-k) Corresponding elemental mapping of NC-650/I_2.

SEM and TEM were employed to characterize the micromorphology of the NC-600, NC-650, and NC-700 materials. As illustrated in **Error! Reference source not found.**a-f, the as-prepared NC-650 exhibits an irregular, porous sheet-like structure. When the carbonization temperature is set at 600°C and 700°C, the morphologies of NC-600 and NC-700 remain sheet-like, with no significant changes observed in the layer thickness. Simultaneously, the microstructure of the NC-650/I_2 composite was investigated via TEM. High-magnification TEM images further confirm the rough

surface and abundant micropores within the sheet-like architecture (**Error! Reference source not found.**g and Fig S1). At various magnifications, the carbon substrate consistently displays a typical and uniform "worm-like" interconnected texture. No distinct long-range ordered graphitic lattice fringes are observed, and the loaded iodine shows no sign of bulk crystalline aggregation; instead, it is well-dispersed within the pores. This amorphous porous microstructure is highly consistent with the high degree of defect characteristics revealed by XRD and Raman spectroscopy. The presence of extensive micropores in NC-650 not only provides a large specific surface area but also accommodates sufficient space for iodine storage. The Energy-dispersive X-ray spectroscopy (EDS) mapping in **Error! Reference source not found.**h-k reveals that carbon (C), nitrogen (N), oxygen (O), and iodine (I) are uniformly distributed throughout the carbon architecture.

Fig. 3a displays the XRD patterns of the NC-600, NC-650, and NC-700 materials, where a broad diffraction peak observed between approximately 20° and 30° corresponds to the characteristic (002) plane of graphitic carbon. Notably, in the XRD pattern of the NC-650/I_2 composite, the (002) diffraction peak at 24° becomes significantly narrower and more intense compared to that of the pristine carbon substrate. This variation does not signify a macroscopic graphitization of the carbon framework. However, it originates from the successful nanoconfinement of iodine. As a heavy element, highly dispersed iodine molecules are restricted within the micropores and mesopores of NC-650. The intense X-ray scattering signal from the encapsulated iodine overlaps with the (002) signal of the carbon matrix, leading to the observed sharpening of the peak. This phenomenon is highly consistent with the drastic reduction in BET pore volume, providing robust cross-evidence for the high-density and ordered confinement of iodine molecules at the sub-nanometer scale. To further evaluate the defect density and degree of graphitization, Raman spectra were recorded. As shown in Fig. 3b, all samples exhibit two distinct characteristic carbon bands: the D-band (1335 cm^{-1}) and the G-band (1585 cm^{-1}), which are attributed to defect-induced disordered carbon and sp^2-hybridized graphitic carbon, respectively. Generally, the degree of graphitization and the structural defect density of carbon materials can be reflected by the intensity ratio of the D-band to the G-band (I_D/I_G), where a higher ratio signifies a lower degree of graphitization and a more pronounced presence of structural defects. After calculation, NC-650 exhibits the highest I_D/I_G ratio (1.017), suggesting that this pyrolysis temperature represents an optimal balance point, which can facilitate the formation of nanoscale

graphitic domains while simultaneously maximizing the density of edge defects. This unique microstructural architecture provides a robust structural foundation for its superior high-rate electrochemical performance. Furthermore, N_2 adsorption-desorption measurements were conducted to investigate the specific surface area (SSA) and pore size distribution (PSD).

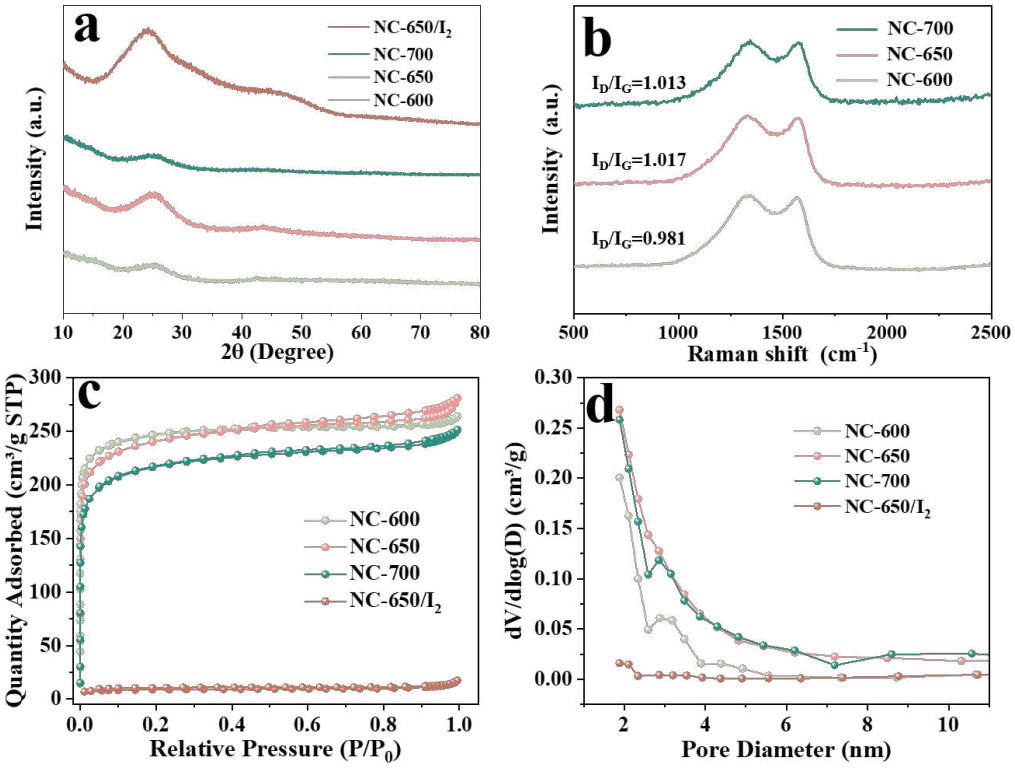

Fig. 3 (a) XRD patterns of NC-600, NC-650, NC-700 and NC-650/I_2; (b) Raman patterns of NC-600, NC-650 and NC-700; (c) N_2 adsorption and desorption isotherms, (d) Pore-size distribution of NC-600, NC-650, NC-700 and NC-650/I_2.

As shown in Fig. 3c, all NC-T materials exhibit Type I isotherms, signifying an abundant microporous structure, which is consistent with the PSD results (Fig. 3d). The PSD curves reveal that the pores are primarily distributed within 1-2 nm. It has been reported that such extensive microporosity can confine iodine atoms within the pores, effectively mitigating the dissolution and diffusion of iodine into the electrolyte, thereby suppressing the polyiodide shuttle effect and enhancing the utilization of active iodine [20, 32, 33]. Based on the BET result, the SSA of NC-650 was calculated to be 992.74 $m^2 g^{-1}$, which is superior to those of NC-600 (882.07 $m^2 g^{-1}$) and NC-700 (830.43 $m^2 g^{-1}$). The larger SSA and rich microporous architecture of NC-650 provide ample space for iodine loading. The N_2 adsorption capacity decreases sharply after iodine loading, with

the pore volume becoming negligible, confirming the successful encapsulation of iodine within the carbon framework.

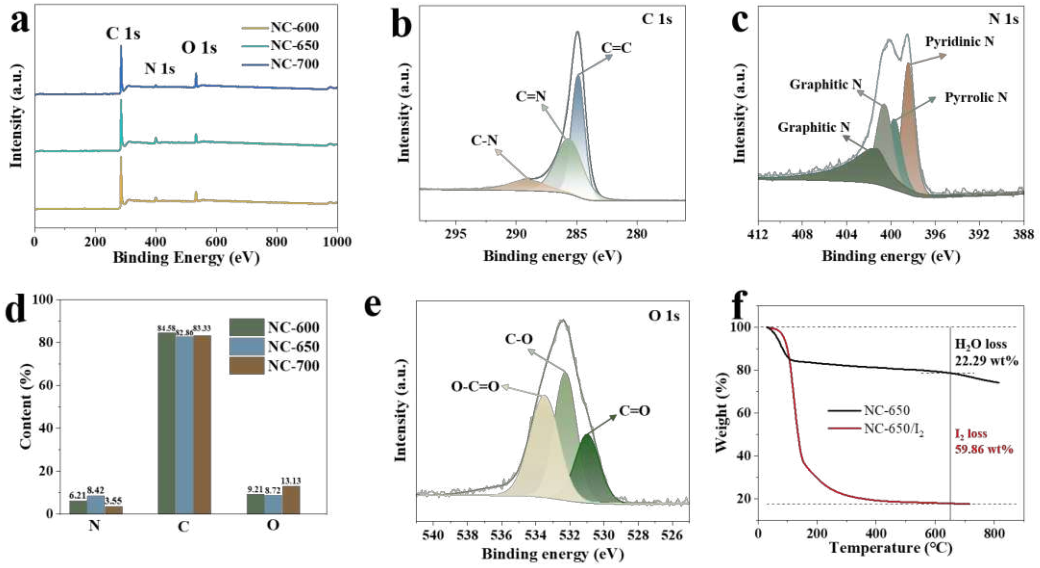

Fig. 4 (a) XPS of samples; (b) C 1s, (c) N 1s and (d) O 1s of NC-650; (e) C, N, and O content of three materials; (f) TGA of NC-650/I_2 and NC-650.

Furthermore, XPS was employed to determine the chemical composition and elemental valence states of all materials. As illustrated in the XPS survey spectra (Fig. 4a), the presence of C, O, and N elements is clearly identified in all samples. Additionally, the high-resolution C 1s spectra (Fig. 4b) exhibit three distinct deconvoluted peaks at 284.9, 285.6 and 288.7 eV, which correspond to C=C, C=N, and C-N bonds, respectively. The existence of C=N and C-N bonds confirm the successful incorporation of nitrogen into the carbon framework. To further elucidate the chemical states of the doped nitrogen, the high-resolution N 1s spectra were deconvoluted. As shown in Fig. 4c, the N 1s spectra of all NC-T samples resolve into four characteristic peaks corresponding to pyridinic-N (398.3 eV), pyrrolic-N (399.8 eV), graphitic-N (400.7 eV), and oxidized-N (402.5 eV). It has been well-documented that pyridinic-N and pyrrolic-N facilitate the surface adsorption of iodine, thereby enhancing iodine utilization and effectively suppressing the iodide shuttle effect, whereas an increased graphitic-N content is conducive to improving the electrical conductivity [37-39]. More importantly, the integration of these active nitrogen sites within the ultra-high surface area microporous network creates a robust dual physical confinement-chemical anchoring mechanism. The strongly electronegative pyridinic and pyrrolic nitrogen dopants alter the local electron density of the carbon framework, generating strong dipole-dipole interactions and chemical

bonding with polar polyiodide species (e.g., I_3^-, I_5^-). When coupled with the stringent spatial restriction provided by the 1-2 nm micropores, this synergistic effect fundamentally limits the transmembrane diffusion of polyiodides, thereby realizing efficient suppression of the shuttle effect and boosting the redox kinetics of iodine. Quantitative XPS analysis reveals that the nitrogen contents in NC-600, NC-650, and NC-700 are 6.21%,8.42% and 3.55%, respectively (Fig. 4d). As the pyrolysis temperature increases from 600 to 700°C, the nitrogen content exhibits a gradual decrease. This is likely attributable to the high volatility of nitrogen-containing ligands at elevated temperatures [35, 36]. The O 1s peak of NC-650/I_2 could be split into three distinct peaks at531.4 (C=O bond), 531.9 eV (C-O bond) and 535.6 eV (O-C=O bond) (Fig. 4e).TGA was performed under a nitrogen atmosphere to determine the iodine content in the NC-T/I_2 composites (Fig. 4f). The initial mass of pristine carbon material decreased by 22.29 wt.%, which is attributed to the evaporation of adsorbed moisture. The actual iodine content in the NC-T/I_2 composites is approximately 42 wt.%. Furthermore, as illustrated in Fig. 4f, the weight loss of iodine occurs as a multi-stage process. The initial loss observed between 100-150°C corresponds to the volatilization of iodine adsorbed on the external surface of the carbon material. In contrast, the weight loss occurring within the 150-400°C range is attributed to the sublimation of iodine molecules infiltrated deep into the micropores. This distinct two-stage behavior arises because surface-bound iodine is more prone to volatilization, whereas iodine sequestered within the internal channels-particularly the micropores—encounters significantly higher diffusion resistance and stronger interaction forces, making it more difficult to remove [34]. This enhanced thermal stability further corroborates the potent physical confinement effect of the NC-T framework.

The electrochemical performances of NC-600/I_2, NC-650/I_2, and NC-700/I_2 were evaluated using CR2032 coin cells to validate the effectiveness of the NC-650/I_2 design. As illustrated in Fig. 5a, the CV curves of all three materials exhibit a well-defined pair of redox peaks, corresponding to the iodine reduction/oxidation and the associated discharge/charge processes. The initial discharge/charge polarization (defined as the cathodic/anodic peak potential difference, ΔV) for NC-600/I_2, NC-650/I_2, and NC-700/I_2 was measured to be approximately 210.3, 137.3 and 164.2 mV, respectively. These results demonstrate that the hierarchical porous structure of NC-650/I_2 is particularly effective in enhancing the activity and reversibility of the I_2 redox reaction. At a scan rate of 1 mV s^{-1}, the surface-capacitive contribution of the NC-650/I_2 cathode reached to 91.3%

(Fig. 5b). The redox kinetics of the electrode were further investigated through CV measurements at various scan rates, as shown in Fig. 5c. As the scan rate increases from 0.1 to 1.0 mV s^{-1}, the CV curves maintain a consistent shape while the cathodic and anodic peaks gradually broaden. Notably, the peaks associated with iodine reduction and oxidation shift toward lower and higher potentials, respectively. For the NC-650/I_2 electrode, the peak potential shift remains minimal even as the scan rate increases, signifying superior iodine redox kinetics, which aligns with previous reports. Additionally, Fig. S2 displays the CV curves for the NC-600/I_2 and NC-700/I_2 electrodes within the same scan rate range (0.1-1.0 mV s^{-1}).

The quantitative relationship between the peak current (i) and the scan rate (v) can be further analyzed using equations (1) and (2).

$$i = av^b \quad (1)$$

$$\log i = b \log v + \log a \quad (2)$$

Where, a is a constant, and the b-value is derived from the slope of the log(i) versus log(v) plot. Specifically, b-value of 0.5 indicates a process primarily governed by ionic diffusion, whereas a value of 1.0 signifies a completely surface-controlled process [40, 41].

EIS measurements and the corresponding fittings further reveal that NC-650/I_2 exhibits a much lower charge transfer resistance (R_{ct}) than its counterparts (Fig. 5d). This reduced R_{ct} is ascribed to the well-developed network of fast charge transport channels. For the discharge process (cathodic peak), the calculated b-value of the NC-650/I_2 electrode (Fig. 5e and Fig. S3) is 0.858, which is notably higher than those of the NC-600/I_2 (0.823) and NC-700/I_2 (0.839) electrodes. This finding reveals that the electrochemical kinetics of the NC-650/I_2 electrode are dominated by rapid surface-controlled behavior. Furthermore, the contribution of capacitive capacity to the total capacity was quantitatively evaluated to elucidate the detailed reaction mechanism.

$$\mathrm{i(v)} = \mathrm{k_1 v} + \mathrm{k_2 v^{\frac{1}{2}}} \quad (3)$$

$$\mathrm{i(v)/v^{\frac{1}{2}}} = \mathrm{k_1\, v^{\frac{1}{2}}} + \mathrm{k_2} \quad (4)$$

Specifically, the total current response i(v) is partitioned into the capacitive-controlled (k_1v) and diffusion-controlled ($k_2 v^{\frac{1}{2}}$) currents, where v represents the scan rate, while k_1 and k_2 correspond to the slope and intercept derived from the linear fitting of $i(V)/v^{\frac{1}{2}}$ versus $v^{\frac{1}{2}}$, respectively [3, 42, 43]. Fig. 5f and S4 quantitatively compare the capacitive contribution ratios of the NC-650/I_2

cathode with those of NC-600/I_2 and NC-700/I_2 as the scan rate increases from 0.1 to 1.0 mV s^{-1}. The NC-650/I_2 electrode exhibits a significantly higher capacitive contribution, with values increasing from 78.44% to 94.68% as the scan rate rises. In contrast, under the same conditions, the NC-600/I_2 and NC-700/I_2 electrodes show lower capacitive contributions, ranging from 70.2% to 89.83% and 75.6% to 91.3%. This distinct difference in pseudocapacitive behavior highlights the superior electrochemical kinetics of NC-650/I_2, where the hierarchical porous structure and nitrogen doping synergistically enhance the surface-controlled charge storage mechanism. The N-doped hierarchical pores not only accommodate the volume expansion of active materials during cycling but also maintain the structural integrity of the electrode, thereby facilitating highly reversible redox reactions. Quantitative analysis reveals that the NC-650/I_2 cathode achieves a maximum capacitive contribution of 91.3% at a scan rate of 1.0 mV s^{-1} (Fig. 5f). This high capacitive contribution originates from the large specific surface area of the NC-650 substrate and the rapid conversion kinetics of iodine species at the N catalytic sites.

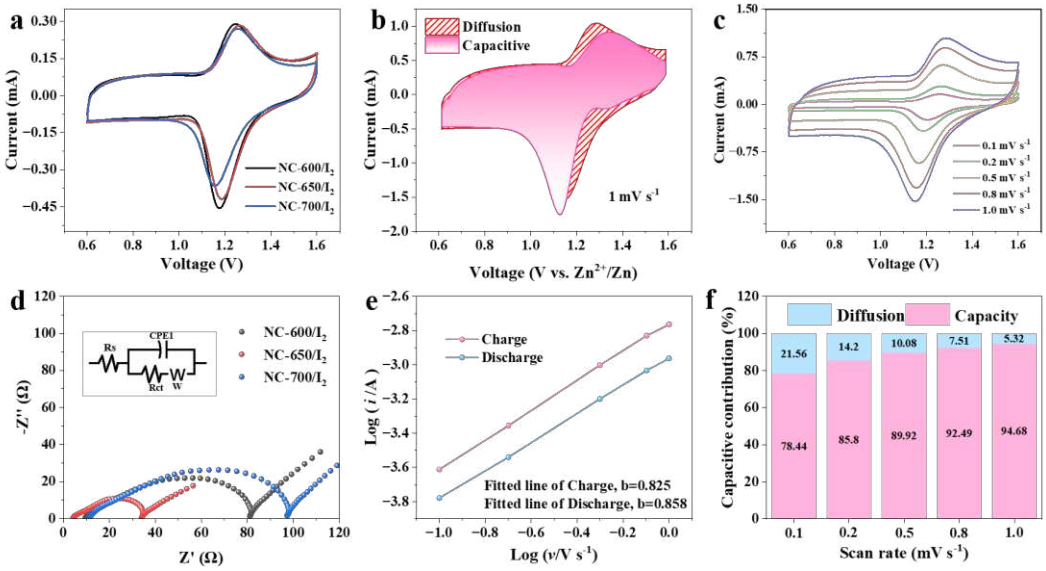

Fig. 5 (a) CV of NC-600/I_2, NC-650/I_2 and NC-700/I_2 with scan rate of 1.0 mV s^{-1}; (b) The capacitive-controlled contribution of NC-650/I_2 at 1.0 mV s^{-1}; (c) CV curves of NC-650/I_2 cathodes at different scan rates from 0.1 to 1 mV s^{-1}; (d) EIS of NC-600/I_2, NC-650/I_2 and NC-700/I_2; (e) CV curves of the corresponding linear relationship between the peak current and the square root of the scan rate for NC-650/I_2; (f) Contribution rate of capacitance capacity of NC-650/I_2.

As shown in **Error! Reference source not found.**a, the galvanostatic charge/discharge (GCD) curves of the NC-650/I_2 cathode demonstrate superior specific capacities across various current densities. Specifically, it delivers discharge specific capacities of 161.49, 150.09, 141.93, and

135.30 mAh g^{-1} at current densities of 0.1, 0.2, 0.5, and 1.0 A g^{-1}, respectively. Notably, when the current density is restored to 0.1 A g^{-1}, the specific capacity recovers to 153 mAh g^{-1}, indicating outstanding rate performance. In addition, the excellent overlap of the charge-discharge performance in the initial three cycles (**Error! Reference source not found.**b) further confirms the excellent reversibility of the NC-650/I_2 electrode. After 200 cycles, the NC-650/I_2 electrode maintains a significantly higher discharge specific capacity compared to the NC-600/I_2 and NC-700/I_2 electrodes (**Error! Reference source not found.**c). This divergence is primarily attributed to the optimized micropore distribution of the NC-650/I_2 framework. The long-term cycling stability was also rigorously evaluated (**Error! Reference source not found.**d). After 1,000 cycles at 1.0 A g^{-1}, the NC-650/I_2 cathode retains a capacity of 135.5 mAh g^{-1} with a retention rate of 88.9%. In contrast, the NC-600/I_2 and NC-700/I_2 electrodes only maintain approximately 109.0 mAh g^{-1} at 1 A g^{-1}. Extended cycling tests (**Error! Reference source not found.**e) further demonstrate the exceptional durability of NC-650/I_2, which exhibits ultra-long-term stability over 3,000 cycles with approximately 83.6% capacity retention and nearly 100% Coulombic efficiency. These results confirm that the superior charge transfer kinetics of NC-650/I_2 stem from its rationally designed N-doped hierarchical porous structure, where the micropore-dominant carbon nanofibers provide abundant electrode/electrolyte interfaces [44]. Consequently, the NC-650/I_2 electrode represents a promising candidate for aqueous zinc-iodine batteries in practical energy storage applications.

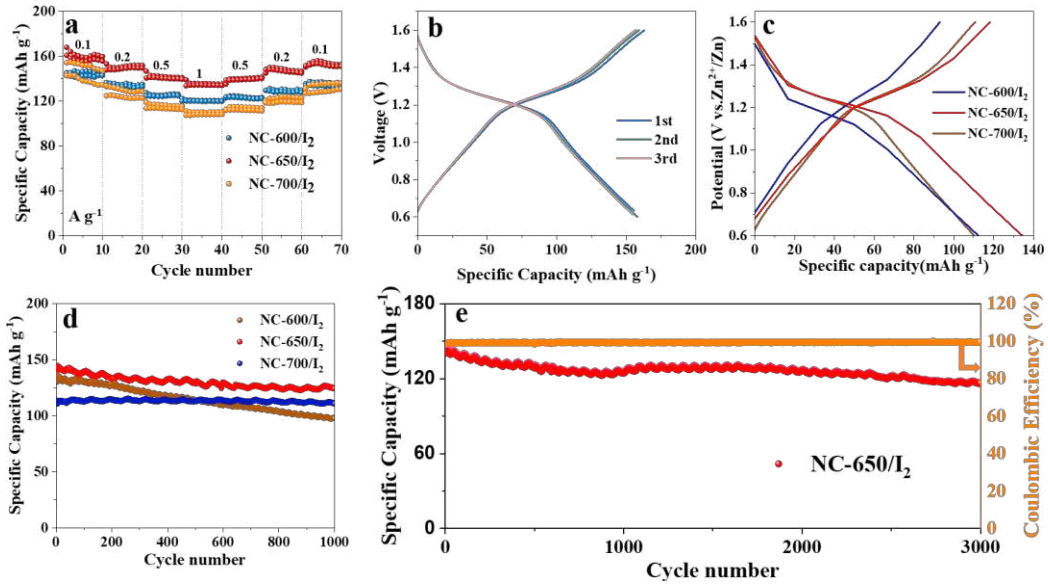

Fig. 6 (a) Rate capability; (b) Performance at 0.1A g^{-1} in the first three cycles of NC-650/I_2; (c) Performance comparison at cycle 200; (d)1000-cycle performance comparison at 1 A g^{-1}; (e) 3000-cycle performance at 1 A g^{-1}

of NC-650/I_2.

4. Conclusion

In summary, the in-situ doped nitrogen atoms impart a robust chemical anchoring effect that synergizes with the physical confinement to effectively suppress the polyiodide shuttle effect and enhance interfacial charge transfer. Benefiting from this rational structural and compositional design, the optimized NC-650/I_2 cathode delivers a superior specific capacity of 161.49 mAh g^{-1} at a current density of 0.1 A g^{-1}. Remarkably, it exhibits outstanding ultra-long cycling stability, maintaining 83.6% of its initial capacity with a Coulombic efficiency consistently near 100% after 3000 cycles at a high current density of 1.0 A g^{-1}. The exceptional electrochemical performance was primarily attributed to its unique microporous structure and N-doped enables NC-650/I_2 to effectively anchor polyiodides, inhibit their diffusion, and thereby achieve efficient iodine conversion. This study provides valuable insights into the structural engineering of porous carbon-based host materials and offers an innovative perspective for developing high-energy-density and long-life aqueous zinc-iodine batteries.

Data availability

Data will be made available on request.

Acknowledgements

This work is financial supported by National Natural Science Foundation of China (Grant No. 52567025), Yunnan Fundamental Research Projects (Grant NO. 202301BE070001-065), Scientific Research Fund Project of Yunnan Provincial Department of Education (2024J0750).

References

[1] BAI C, JI K, FENG S, et al. An intrinsically stretchable aqueous Zn-MnO_2 battery based on microcracked electrodes for self-powering wearable electronics [J]. Energy Storage Materials, 2022, 47: 386-393.

[2] ZHAO W, JIN G, XU Z, et al. Recent advances in electrolyte engineering for aqueous zinc–iodine batteries: challenges and strategies for optimization [J]. Electrochemical Energy Reviews, 2026, 9:7.

[3] SUN M, WEI L, PENG J, et al. BN/rGO nanocomposites as efficient iodine hosts for triiodide

confinement and accelerated I_2/I^- redox kinetics in zinc-iodine batteries [J]. Journal of Energy Storage, 2025, 137, 118643.

[4] YE J, TIAN W, DU Y, et al. Defect-engineered ZIF-derived carbon hosts for long-life aqueous zinc-iodine batteries [J]. Advanced Functional Materials, 2025, 35(47): 2509582.

[5] XU S, MA J, JIA H, et al. Preparation of porous carbon derived from a lignin-based polymer through $ZnCl_2$ activation for effective capture of iodine [J]. International Journal of Biological Macromolecules, 2025, 294,139412.

[6] XU H, ZHANG R, LUO D, et al. Polarity coupling in biphasic electrolytes enables iodine/polyiodide co-extraction for portable Zn-iodine batteries following a liquid–liquid conversion route [J]. Energy & Environmental Science, 2025, 18(15): 7447-7459.

[7] WANG L, GUAN J, LI N, et al. Amine-functionalized MIL-125 separator and MOF-derived carbon host for high-performance aqueous zinc-iodine batteries [J]. Advanced Energy Materials, 2025, 15(45): e04201.

[8] QI D, JIANG H, CHEN X, et al. Design Strategies, Challenges, and prospects of nanomaterials for aqueous Zn-iodine batteries [J]. ACS Nano, 2025, 19(27): 24592-24620.

[9] ZHENG X, SHEN H, WEI J, et al. Wood-derived carbon as self-supporting cathode and current collector for static zinc-iodine batteries [J]. Bioresource Technology, 2025, 434, 132779.

[10] LIU Y, WU X, BANDO Y. Toward highly durable aqueous zinc ion batteries: a review of MOFs/MOF-derived cathode materials [J]. Inorganic Chemistry Frontiers, 2025, 12(12): 3959-3980.

[11] LI H, HUANG B, CHUAI M, et al. Dual-plating aqueous Zn–iodine batteries enabled via halogen-complexation chemistry for large-scale energy storage [J]. Energy & Environmental Science, 2025, 18(7): 3160-3168.

[12] HOU Y, WEI L, SUN N, et al. Mesoporous dominated porous carbon with high nitrogen and phosphorus doping levels toward high area capacity zinc-iodine batteries [J]. Journal of Energy Storage, 2025, 120, 116495.

[13] YANG X, FAN H, HU F, et al. Aqueous zinc batteries with ultra-fast redox kinetics and high iodine utilization enabled by iron single atom catalysts [J]. Nano-Micro Letters, 2023, 15(1): 126.

[14] GUO G, DAI Q, LI W, et al. Intercatenation weaves MOFs with conductive networks as iodine

hosts for zinc-iodine batteries [J]. Chemical Engineering Journal, 2025, 514, 163100.

[15] YAN W, LIU Y, QIU J, et al. A tripartite synergistic optimization strategy for zinc-iodine batteries [J]. Nature Communications, 2024, 15(1), 9702.

[16] ZHANG Y, ZHANG X, LI X, et al. Enabling high-areal-capacity zinc-iodine batteries: Constructing high-density microporous carbon framework with large surface area [J]. Journal of Alloys and Compounds, 2024, 976, 1734041.

[17] LI M, WU J, LI H, et al. Suppressing the shuttle effect of aqueous zinc–iodine batteries: progress and prospects [J]. Materials, 2024, 17(7): 1646.

[18] XU H, YANG W, LI M, et al. Advances in aqueous zinc ion batteries based on conversion mechanism: challenges, strategies, and prospects [J]. Small, 2024, 20(27), 2310972.

[19] LI N, YANG Z, LI Y, et al. Size confinement strategy effect enables advanced aqueous zinc–iodine batteries [J]. Advanced Energy Materials, 2024, 14(44), 2402846.

[20] BAI Z, WANG G, LIU H, et al. Advancements in aqueous zinc-iodine batteries: a review [J]. Chemical Science, 2024, 15(9): 3071-3092.

[21] PAN G X, WANG Z Y, ZHANG J C, et al. Porous carbon-coated Fe-doped MnO as high-performance cathode for aqueous zinc ion batteries [J]. Energy Technol-Ger, 2025, 13(4): 2401690.

[22] LI Y, GUO X, WANG S, et al. Nano/micro metal-organic framework-derived porous carbon with rich nitrogen sites as efficient iodine hosts for aqueous zinc-iodine batteries [J]. Advanced Science, 2025, 12(26): 2502563.

[23] LIU T, WANG H, LEI C, et al. Recognition of the catalytic activities of graphitic N for zinc-iodine batteries [J]. Energy Storage Materials, 2022, 53: 544-551.

[24] YANG L, LI J, ZHOU Y, et al. Towards high-performance supercapacitors with cellulose-based carbon for zinc-ion storage [J]. Journal of Energy Storage, 2022, 50, 104252.

[25] LI X Y, WANG L, FU Y H, et al. Optimization strategies toward advanced aqueous zinc-ion batteries: From facing key issues to viable solutions [J]. Nano Energy, 2023, 116, 108858.

[26] JI Y, XU J, WANG Z, et al. Nitrogen-doped litchi-shell derived porous carbon as an efficient iodine host for zinc-iodine batteries [J]. Journal of Electroanalytical Chemistry, 2023, 931, 117188.

[27] YU J, LIU C, HUANG H, et al. One-step activation towards N/O-co-doped carbon for iodine

confinement-conversion in Zn-I_2 batteries [J]. Journal of Energy Storage, 2026, 154, 121202.

[28] ZHU M, CHEN J, CHANG J, et al. Al-doped nitrogen-doped carbon-loaded vanadium nitride vanadium trioxide heterojunctions composites as cathode material for high-performance aqueous zinc ion battery [J]. Electrochimica Acta, 2026, 553, 148290.

[29] QIAN Y, CHANG G, HUANG C, et al. Three-pronged approach enhances porous carbon spheres for high-performance aqueous zinc-iodine batteries [J]. ACS Sustainable Chemistry & Engineering, 2025, 13(30): 12057-12066.

[30] LI S, ZHOU K, LI X, et al. Green synthesis of high-iodine-adsorbing porous biomass-derived carbon for shuttle-free aqueous zinc-iodine batteries [J]. Journal of Energy Storage, 2026, 152, 120863.

[31] ZHANG X, LI X, SUN M, et al. Nitrogen-doped oxygen-rich porous carbon framework towards aqueous zinc ion hybrid capacitors and zinc-iodine batteries [J]. Journal of Electroanalytical Chemistry, 2024, 952, 117965.

[32] XU Y, LI Y, JIA H, et al. Hierarchical micro-mesoporous carbon firmly confined iodine for high performance zinc-iodine batteries [J]. Materials Letters, 2023, 353, 135241.

[33] QI Y, LIU Q, WANG B, et al. Role of high-defect biocarbon for achieving iodine efficient anchoring and rapid conversion in zinc-iodine battery [J]. Physica Scripta, 2025, 100(8), 085995.

[34] JIANG C, HU F, ZHANG H, et al. Supramolecular channels via crown ether functionalized polyaniline for proton-self-doped cathode in aqueous zinc-ion battery [J]. Journal of Colloid and Interface Science, 2024, 669, 637-646.

[35] LI M, ZHAO G, YU D, et al. Chitin derived carbons as surface chemical adsorption host for high performance aqueous zinc-iodine batteries [J]. ChemistrySelect, 2025, 10(17): e202405961.

[36] MOU J, LIU T, LI Y, et al. Hierarchical porous carbon sheets for high-performance room temperature sodium–sulfur batteries: integration of nitrogen-self-doping and space confinement [J]. Journal of Materials Chemistry A, 2020, 8(46): 24590-24597.

[37] ZHU L, GUAN X, LI P, et al. Waste coffee grounds-derived micropores carbon framework as an efficient iodine host for zinc iodine battery [J]. Energy & Environmental Materials, 2025, 8(5): 163-170.

[38] YU D, KUMAR A, NGUYEN T A, et al. High-voltage and ultrastable aqueous zinc–iodine battery enabled by N-doped carbon materials: revealing the contributions of nitrogen configurations [J]. ACS Sustainable Chemistry & Engineering, 2020, 8(36): 13769-13776.

[39] WANG Y, PAN T, ZHANG S, et al. MOF-based electrode materials for aqueous zinc-ion batteries: design strategy and future challenges [J]. Inorganic Chemistry Frontiers, 2025, 12(8): 2988-3017.

[40] PAN X, SONG K, ZHU Y, et al. Functional nanoarchitectonics with metal-organic framework derived porous carbon as an efficient iodine host for high performance aqueous zinc-iodine batteries [J]. Journal of Electroanalytical Chemistry, 2026, 1000, 119645.

[41] LI C, YAN L, LV M, et al. Vesicular porous carbon with outstanding electrochemical performances in Zn-based devices: extracted from asphalt and wood precursors [J]. Journal of Energy Storage, 2025, 113, 115561.

[42] WEN H, WEN H, SUN Y, et al. The frontiers of aqueous zinc–iodine batteries: A comprehensive review on mechanisms, optimization, and industrial prospects [J]. Advanced Functional Materials, 2025, 35(31): 2500323.

[43] CHEN C, LIU C, HUANG H, et al. Green potassium salt activation of biomass carbon unlocks high-performance zinc-iodine batteries [J]. Electrochimica Acta, 2026, 559, 148584.

[44] XU J, WANG J, GE L, et al. ZIF-8 derived porous carbon to mitigate shuttle effect for high performance aqueous zinc–iodine batteries [J]. Journal of Colloid and Interface Science, 2022, 610, 98-105.

Supplementary Files

This is a list of supplementary files associated with this preprint. Click to download.

- Supplementarymaterial.docx